Global potential energy surface and dynamics for the OH + CH_3OH reaction

J. Espinosa-Garcia* and C. Rangel

Área de Química Física and Instituto de Computación Científica Avanzada

Universidad de Extremadura, 06071 Badajoz (Spain)

*E-mail: joaquin@unex.es

ABSTRACT

Using as functional form a combination of valence bond and mechanic molecular terms a new full-dimensional potential energy surface was developed for the title reaction, named PES-2022, which was fitted to high-level *ab initio* calculations at the coupled-cluster singles, doubles and perturbative triples-F12 explicitly correlated level on a representative number of points describing the reactive system. This surface simultaneously describes the two reaction channels, hydrogen abstraction from the methyl group (R1 path) and from the alcohol group (R2 path) of methanol to form water. PES-2022 is a smooth and continuous surface which reasonably describes the topology of this reactive system from reactants to products, including the intermediate complexes present in the system. Based on PES-2022 an exhaustive dynamics study was performed using quasi-classical trajectory calculations under two different initial conditions: at a fixed room temperature, for direct comparison with the experimental evidence and at different collision energies, to analyse possible mechanisms of reaction. In the first case, the available energy was mostly deposited as water vibrational energy, with the vibrational population inverted in the stretching modes and not inverted in the bending modes, reproducing the experimental evidence. In the second case, the analysis of different dynamics magnitudes (excitation functions, product energy partitioning and product scattering distributions), allows us to suggest different mechanisms for both R1 and R2 paths: a direct mechanism for the R2 path versus an indirect one, related with "nearly-trapped" trajectories in the intermediate complexes, for the R1 path.

I. INTRODUCTION

The quantitative description of state-to-state dynamics properties comparable to experiments needs full dimensional quantum mechanical (QM) calculations based on accurate and global potential energy surfaces (PES). In the case of polyatomic systems this goal is far from being achieved. Recently, our group has analysed this problem[1] by studying the current status of the X + C_2H_6 [X≡ H, F(^{2}P), Cl(^{2}P), O(^{3}P), OH] hydrogen abstraction reactions. We concluded that the experiment/theory comparison worsens when we go from macroscopic properties (average properties, such as the rate constants) to microscopic properties (state-to-state properties, such as product vibrational distribution).

The reaction of methanol with the hydroxyl radical is an oxidative process of great importance in cold interstellar space, atmosphere and combustion (i.e., very-low, low and high temperatures)[2-5] and has been widely studied from different perspectives: mechanism, kinetics and dynamics, using experimental and theoretical tools. With respect to the mechanism, this reaction proceeds through a common reactant complex (RC) and from here two paths appear (R1 and R2), with their respective saddle points (SP) and product complexes (PC), to finish in the respective products, $CH_2OH + H_2O$ and $CH_3O + H_2O$, respectively,

$$OH + CH_3OH \rightarrow RC \begin{cases} \rightarrow SP1 \rightarrow PC1 \rightarrow CH_2OH + H_2O & (R1) \\ \rightarrow SP2 \rightarrow PC2 \rightarrow CH_3O + H_2O & (R2) \end{cases}$$

i.e., the OH free radical abstracts an H atom from the methyl group (R1 path) or from the hydroxyl group (R2 path) of methanol, where the R2 reaction contributes in lesser measure.[6,7] Both paths are strongly exothermic, $\Delta H_R^o(298K)$ = -22.74±0.08 and -13.62±0.08 kcal mol^{-1}, respectively, from the corresponding standard enthalpies of formation[8] and therefore, low barrier heights are expected.

Theoretically, different groups analysed this reaction using different tools, *ab initio* or density functional theory (DFT).[9-20] Focussing on the most recent and accurate results, Galano et al.[11] used the coupled-cluster with single, double and triple (perturbative) excitations, CCSD(T), level on optimized geometries with a DFT method to characterize the stationary points. They found a reactant complex and the corresponding saddle points for the R1 and R2 reactions, with barriers of 2.1 and 3.1 kcal mol^{-1}, respectively. Xu and Lin[12] used also the CCSD(T) level to obtain the energies, but now based on optimized

geometries at the Møller-Plesset, MP2, level. In addition to the reactant complex, they also reported a product complex for each path and barriers of 1.0 and 3.6 kcal mol^{-1}, respectively. In the theoretical study of Siebrand et al.[14] a DFT method was used and only the reactant complex was reported, where the corresponding barrier heights were 0.5 and 2.5 kcal mol^{-1}, respectively, while Gao et al.[15] reported barriers of 1.5 and 4.0 $kcalmol^{-1}$. Nguyen et al.[17] reported a master equation simulation for the title reaction, where the stationary points were characterized at the CCSD(T) level using a complete basis set. They reported barriers of 1.0 and 3.6 kcal mol^{-1} for R1 and R2 reactions, respectively. These are the most accurate results, although the authors concluded that "In this case, at least, CCSD(T) does not appear to be enough". Recently, Ali et al.[19] used a combination of CCSD(T) and DFT methods to analyse the reaction. They reported a common reactant complex, stabilized by 4.97 kcal mol^{-1} with respect to the reactants, and product complexes for each reaction path, R1 and R2. The corresponding barrier heights are 0.84 and 2.5 kcal mol^{-1} (zero point corrected values). Finally, Roncero et al.[16] reported the first full-dimensional potential energy surface, PES, for this reaction, which is a many-body (MB) expression fitted to ~200 000 *ab initio* points obtained at the CCSD(T)-F12 explicitly correlated method using a basis set of quality double-zeta. The MB surface gives barriers of 2.1 and 6.7 kcal mol^{-1}, respectively, reproducing the *ab initio* information used in the fitting process, but in disagreement with recent and accurate *ab initio* results, with values in the range 1.0-1.5 and 3.6-4.0 kcal mol^{-1}, respectively. In addition, the MB surface does not reproduce the imaginary vibrational frequency at the saddle point, especially for the R1 reaction. So, while for the R2 reaction the values of this magnitude are 2431 i versus 2263 i cm^{-1} using respectively *ab initio* data or the MB surface, for the R1 reaction the differences are larger, 823 i versus 1576 i cm^{-1}.

In the present theoretical work, we reanalyse this reactive system by using high-level *ab initio* calculations, and based on this information we developed a new full-dimensional PES using a different strategy from that used by Roncero et al.[16] In our case, the PES is constructed as a VB/MM surface, i.e., a valence bond function augmented with molecular mechanic terms. This new surface, named PES-2022, has a flexible character to represent different molecular motions, stretching, bending, torsions and long-range interactions; it evolves smoothly from reactants to products, and given that it is based on physically intuitive concepts, it requires less computational effort. This paper is organized as follows. In Section II we describe the new PES-2022 surface. All stationary points on the R1 and R2 paths are optimized and characterized (using harmonic vibrational

frequencies) using high level electronic structure calculations. This information, together with the description of the corresponding reaction paths from reactants to products, is used to fit the new PES-2022, which simultaneously describes the R1 and R2 paths. Section III is devoted to a description of the dynamic computational details using quasi-classical trajectory (QCT) calculations. The results of the dynamics study are shown in Section IV and compared with the only experimental evidence.[21] Finally, the main conclusions are summarized in Section V.

II. POTENTIAL ENERGY SURFACE

In general terms, the construction of an analytical PES consists of three main steps: i) the development of a functional form representing all nuclei motions in the reactive system, ii) the fitting process, and iii) the input data used in the previous step, i.e., the electronic structure calculations describing the reactive system.

Beginning with the input data, the geometries and vibrational frequencies of all stationary points (reactants, products, saddle points and intermediate complexes) for both R1 and R2 paths and, in addition, 60 points describing each minimum energy paths, were calculated using high level *ab initio* calculations. The corresponding energies were obtained using a single-point method, i.e., the geometries and vibrational frequencies were calculated using the couple-cluster with single, double and triple (perturbative) excitations with basis sets of triple-zeta quality, CCSD(T)/cc-pVTZ, and based on these geometries the energy is improved using the explicitly correlated method with a larger basis set, CCSD(T)-F12/aug-cc-pVTZ. All *ab initio* calculations were performed using the Gaussian16[22] and Molpro[23] program packages. Some previous theoretical studies[14,15] noted a high multi-reference character especially for the R2 path, which presents a high T1 diagnostic,[24] ~ 0.05, in these studies. It is known[25] that T1 values larger than 0.02 or 0.045 for closed-shell and open-shell systems, respectively, suggest that a multi-reference method might be needed. In the present work, based on the saddle point geometries optimized at the CCSD(T)/cc-pVTZ level, the T1 diagnostic gives values of 0.022 and 0.029, for R1 and R2 paths respectively, showing that a single-reference method is suitable. The differences with the previous studies is unclear, but we suggest that they could be due to the different level of optimization of the geometries, DFT,[15] or the use of basis set of quality double-zeta.[16]

Following the strategy used in our group in polyatomic reactions (see, for instance, recent references[26-28]) the functional form of the new surface was developed as a valence bond

function augmented with molecular mechanic terms (VB/MM). This surface is formed by a set of terms describing all the stretching motions in the reactive system (C-H, C-O, O-H), V_{stret}, the in-plane bending, V_{ip}, and the out-of-plane bending, V_{op}, motions, the torsional motion around the C-O bond in methanol, V_{tor}, and finally the long range interactions to describe the intermediate complexes in the entrance (reactant complex, RC) and in the exit (product complexes, PC1 and PC2) channels for each R1 and R2 paths. Each term in the surface depends on a set of adjustable parameters, which are directly related with physically intuitive concepts, such as bond length, valence angle, dihedral angle or dissociation energy. For instance, the difference between the dissociation energy of the formed (H-O) and broken (C-H or O-H, depending on the R1 or R2 path) bonds corresponds to the respective energy of reaction. A priori, these VB and MM terms represent a rigid description of the reactive system and therefore, to ensure smooth changes in the polyatomic system, from reactants to products, a set of switching functions are included in the potential, which are hyperbolic tangent functions. In total, 83 adjustable parameters are need to describe the complete system. Note that the new PES is symmetric with respect to the permutation of the three equivalent hydrogen atoms in methanol and simultaneously describes both R1 and R2 paths. A term-by-term detailed description can be found in our previous work on the H + CH_3OH reaction, which also evolves on two paths; H attacks the CH_3 or the OH of methanol,[28] and to avoid unnecessary repetitions they are not presented here. The new terms included in the present work with respect to the previous one,[28] are a Morse potential and a harmonic bending potential,[26] to describe the water product formed, V_{H2O}, and a van der Waals potential,[28] V_{vdw}, to describe long range interactions. In sum, the new potential is developed as,

$$V = V_{stret} + V_{ip} + V_{op} + V_{tor} + V_{H2O} + V_{vdw} \quad (1)$$

Finally, the 83 parameters are fitted to the input data, which represents the third step of the process. This process is simultaneously performed for both R1 and R2 paths. Taking advantage of the physically intuitive character of the terms of the potential, the fitting process is divided in four iterative steps. We begin with the easiest step, the description of the reactants and products: geometry, vibrational frequencies and energy of reaction, which is directly related with the difference of the dissociation energies for the formed and broken bonds: O-H and C-H for the R1 path, and O-H and H-O for the R2 path. The following step is the description of the respective saddle points, SP1 and SP2. In this step, special attention is paid to the barrier height and the imaginary vibrational frequency, related with the curvature of the path in this point. The description of the reaction path

from reactants to products for each path (R1 or R2) represents the third step of the fitting process. In this step, we try to reproduce the falls to reactants (smooth) and products (pronounced) from the respective saddle point. Intimately related to this step is the description of the intermediate complexes in the entrance and exit channels, which represents the fourth step of the process. The adjustable parameters defining the van der Waals term help in this task. These four steps represent the first iteration and so we obtain a first set of 83 adjustable parameters. Obviously, the fitting process is iteratively repeated until a reasonable agreement is reached with the input data. This iterative process is time consuming and tedious, and although we developed a least-square method,[30] which uses energies, gradients and Hessians to obtain the best set of parameters, the complete process is not automatic, and finally a trial-and-error hand-made process is needed. The new PES-2022 surface describing both paths, R1 and R2, will be available in the POTLIB library.[31]

III. DYNAMICS TOOLS: QUASI-CLASSICAL TRAJECTORY SIMULATIONS

When the reactive system is a large polyatomic system, quantum mechanical (QM) calculations are prohibitive and quasi-classical trajectory (QCT) calculations represent an economical and useful alternative, in spite of their classical nature. Using the new PES-2022 surface, QCT calculations were performed at two different initial conditions: at a fixed temperature of 298 K, to compare with the only dynamics experimental study,[21] and at different collision energies in the range 1-10 kcal mol^{-1}. The QCT input parameters in both conditions are summarized in Table 1. From the QCT outcome, i.e., Cartesian coordinates and momenta at the end of each reactive trajectory, a series of dynamical properties can be obtained: i) The reaction cross section, at T=298K or at each collision energy, is given by

$$\sigma_r(T/E) = \pi b_{max}^2 \frac{N_r}{N_T} \quad (1)$$

b_{max} being the maximum impact parameter (Table 1), N_r the number of reactive trajectories and N_T the number of total trajectories run. In the present work, given the number of trajectories, the error in $\sigma_r(T/E)$ is <3%, i.e., practically negligible and therefore it is not reported in the remainder of the text. ii) The scattering angle distribution between the H_2O product and the OH reactant was obtained by binning the range θ=0-180º into 18 equidistant bins of 10º. In this notation θ=0º is associated with a rebound

scattering, while θ=180º is associated with a forward scattering. To obtain scattering comparable with experiments, the DCSs (differential cross sections) are used which are fitted using Legendre polynomials.[34] iii) The product energy distribution is directly obtained from the QCT outcome, which reports the relative translational energy between the products, E^{trans}, and the vibrational and rotational energies of the products, E^{vib}_{CH2OH} (E^{vib}_{CH3O}), E^{rot}_{CH2OH} (E^{rot}_{CH3O}), E^{vib}_{H2O} and E^{rot}_{H2O}, depending on the R1 or R2 paths. At 298 K Butkovskaya and Setser[21] experimentally reported the H_2O vibrational distribution in the stretching and bending motions. However, these a_1-a_3 actions for the H_2O product are not directly obtained from the QCT outcome. They can be calculated using the normal mode analysis, the NMA method, developed in our group.[35] These actions are associated with symmetric stretching (ν_1 = 3678 cm^{-1}), bending (ν_2 = 1602 cm^{-1}) and antisymmetric stretching (ν_3 = 3732 cm^{-1}) of the common water product. Obviously, these actions are real numbers and they are rounded to their nearest integer, n_1-n_3.

Finally, given the classical nature of the QCT calculations, a known problem is the zero-point energy (ZPE) violation, and here we have considered two approaches: a) all reactive trajectories are considered in the analysis (All approach), and b) reactive trajectories with vibrational energy of each product (CH_2OH and H_2O for R1 path, and CH_3O and H_2O for R2 path) lower than their respective ZPEs are discarded in the analysis (DZPE approach, double ZPE approach). Obviously, the latter is a drastic approach, which reduces the number of reactive trajectories in the final analysis. Note that the QCT calculations were performed using the Venus96 code.[32,33]

IV. RESULTS AND DISCUSSION

a) Potential energy surface. Comparison to *ab initio* input data. Figure 1 is a schematic representation of the two R1 and R2 paths for the OH + CH_3OH surface showing the comparison of the stationary-point relative energies obtained on the analytical PES with the *ab initio* CCSD(T)-F12/aug-cc-pVTZ level used in the fitting, which is simply a test of self-consistency. In general, the new PES-2022 surface reproduces the *ab initio* information used in the fitting process. The classical energies of reaction are well reproduced, -22.10 versus -22.05 kcal mol^{-1} for the R1 path and -13.24 versus -12.50 kcal mol^{-1} for the R2 path. These values are also in concordance with the standard enthalpies of reaction, obtained from the corresponding enthalpies of formation,[8] –22.74 and -13.62 kcal mol^{-1}, respectively. The new PES-2022 correctly describes the

presence of a common reactant complex in the entrance channel, stabilized by 4.87 kcal mol^{-1} with respect to the reactant, and the corresponding product complexes in the exit channel, stabilized by 4.86 and 4.90 kcal mol^{-1} with respect to the respective products for the R1 and R2 paths, respectively. A very sensitive parameter describing the topology of the PES is barrier height. The *ab initio* barriers, 1.24 and 3.84 kcal mol^{-1} for the R1 and R2 paths, are well reproduced by the PES-2022 surface, 1.42 and 3.66 kcal mol^{-1}, respectively. These values satisfactorily simulate recent and accurate values in the literature.[12,15,17] These barriers are associated with the corresponding imaginary vibrational frequency, showing the curvature of the reaction path. The PES-2022 frequencies, 858 i and 2176 i cm^{-1}, for the R1 and R2 paths, respectively, reasonably simulate the *ab initio* information, 891 i and 1991 i cm^{-1}. Other theoretical results (*ab initio* or DFT)[11,12,14,16] from the literature show a wide range of values: 437 i-1420 i cm^{-1} for the R1 path and 1737 i-2958 i cm^{-1} for the R2 path, showing that this property is difficult to describe. The MB surface of Roncero et al.[16] gives values of 1576 i and 2263 i cm^{-1}, respectively, which differ from the *ab initio* values used in their fitting, especially for the R1 path and from the present CCSD(T)/cc-pVTZ results.

Figure 2 shows the R1 and R2 reaction paths for the PES-2022 and the *ab initio* input data at the CCSD(T)-F12/aug-cc-pVTZ level. PES-2022 reasonably simulates the entrance channel for both paths, with the largest differences in the exit channel for the R1 path, about 3 kcal mol^{-1}. However, considering all points in the fitting, the overall root-mean-square error (RMSE) is 0.7 kcal mol^{-1}, less than the chemical accuracy (~1 kcal mol^{-1}). Finally, a global vision of both R1 and R2 paths is shown in Figure 3, which represents the 2D contour plots for both paths using the PES-2022 surface. They represent the breaking C-H (R1 path) or O-H (R2 path) and the formed (H-O of water) bonds keeping the remaining coordinates fixed in the respective saddle points. These contour plots are useful because they show the continuous, smooth and differentiable character of the new PES.

In sum, after this analysis, we would like to point out that the present analytical full-dimensional PES-2022 is the most accurate today to describe the multi-channel reaction between methanol and the hydroxyl radical, although there is still room for improvement, especially in the exit channels. However, we think that this deficiency in the exit channels will have little or no influence on the dynamical description of the reactive system.

Next, we analyze the dynamics information obtained based on the PES-2022 surface. As previously noted, the QCT calculations were performed at two different initial conditions:

at a temperature fixed of 298 K, to compare with the only dynamics experimental study,[21] and at different collision energies in the range 1-10 kcal mol^{-1}.

b) QCT results at 298 K. Comparison with experiments. Experimentally, Butkovskaya and Setser[21] studied water-forming in the title reactions at 298 K using the infrared chemiluminiscence technique. They reported i) that the fraction of energy deposited as water vibrational energy is 0.44, although nothing is said about other energy distributions, rotation or translation, and ii) that the water product vibrational distribution is inverted for the stretching modes, $P_{1,3}(0:1:2) = 35:49:16$, while it is significantly broad for the bending excitation. Note that the data correspond to the R1 reaction, $CH_2OH + H_2O$, while information on the R2, $CH_3O + H_2O$, is only speculative. Table 2 lists the QCT product energy partitioning at 298 K, together with the experimental data. With respect to the R1 reaction, the present QCT results reproduce the water vibrational fraction, 0.44, with a small fraction as translation, 0.15. However, the picture for the R2 path is very different. In this case, the largest fraction of energy is deposited as translation, 0.41, while the fraction as water vibrational energy is only of 0.27. Taking into account that in our theoretical calculations the branching ratio, R1/R2, is 0.81/0.19 at 298 K, the fraction of energy as water vibration gives an average value of 0.41, reproducing the experimental evidence. In addition, this branching ratio reproduces the experimental data.[6,7,36] These authors also reported experimentally the water product vibrational distribution. The vibrational actions are denoted (n_{OH}, $n_{bending}$, n_{OH}) associated with the symmetric stretch, bending and antisymmetric stretch vibrational modes (vibrational frequencies of $\nu_1 = 3678$, $\nu_2 = 1602$ and $\nu_3 = 3732$ cm^{-1}) for the H_2O product, using the PES-2022 surface. At this point it is important to note that due to collisional coupling of populations in ν_1 and ν_3 levels experimental populations are assigned to the ($v_{1,3}$,v_2) states in H_2O and therefore the QCT calculated populations must be combined in the same way for comparison with experimental results. So, $v_{1,3} = v_1+v_3$ and v_2 refer to combined stretch and bend modes in water, respectively. The total available energy to the products is about 25 and 16 kcal mol^{-1} for the R1 and R2 paths, respectively. These values are obtained as a sum of the collision energy, E_{coll} ~ 1 kcal mol^{-1} (which is obtained in the present QCT study from an energy distribution at 298 K with the most probable values between 0.5 and 1.5 kcal mol^{-1}); the methanol rotational energy ~0.9 kcal mol^{-1}, which is obtained by thermal sampling at 298 K, and finally the 0K enthalpy of reaction, -22.6 and -13.8 kcal mol^{-1} for R1 and R2 paths, respectively. Considering these available energies and the

water vibrational frequencies, a low vibrational excitation is expected in all vibrational modes, up $n_{OH} = 2$ and $n_{bending} = 5$ for the R1 path and up $n_{OH} = 1$ and $n_{bending} = 3$ for the R2 path. These excitations correspond to pure stretching and bending vibrational excitations, but obviously stretching-bending combined excitations are possible, which complicate the theory/experiment comparison. Table 3 lists the water population distributions obtained in the present QCT study for the R1 and R2 paths, together with the experimental evidence[21] for comparison (in this case, only the R1 path results are reported). The QCT results reproduce the $P_{1,3}(n)$ and $P_2(n)$ statistical distributions experimentally found, where the H_2O product vibrational population is inverted in the stretching modes and not inverted in the bending mode. This good agreement with experiments in the state-to-state dynamical properties analyzed, fraction of energy deposited as water vibrational energy and water population distributions, lends confidence to the methodology used, which is a combination of PES-2022, QCT and NMA. Even the persistent theory/experiment differences can be explained by limitations of the theoretical tools used, without discarding experimental uncertainties. For instance, uncertainties of ±10% in the stretching distributions, while the bending distributions are less reliable due to experimental difficulties in the assignation of the bending populations in the $v_{1,3} = 0$ state.[21]

c) QCT results at different collision energies. Unlike the results at 298 K no experimental data have been reported at different collision energies, and so comparison is not possible. Therefore, the present QCT results acquire a predictive character, to be confirmed (or not) by future experiments.

Figure 4 plots the excitation function, i.e., the cross section as a function of the collision energy in the range 1-10 kcal mol^{-1}, for both R1 and R2 paths. Firstly, the effect of the QCT constraint (DZPE approach) is more pronounced in the R2 path ($CH_3O + H_2O$ products) than in the R1 path ($CH_2OH + H_2O$ products). Secondly, both excitation functions show the typical threshold behaviour increasing with energy of the reactions with barrier, however, they present a different picture. So, while in the R1 path the cross section increases with the collision energy, in the R2 path the cross section increases up to collision energy of ~7 kcal mol^{-1} and then decreases. This behaviour could be related with the variation of the impact parameters for both paths. Thus, while in the R1 path the impact parameter increases with the collision energy, for the R2 path it has the opposite

tendency. In this second case, the balance between impact parameter and increase of the reactive trajectories with the collision energy, gives the behaviour observed.

The product energy partitioning (vibration, rotation and translation) for both R1 and R2 paths are listed in Table 4, where unfortunately no experimental data are available for comparison. While in the R1 path the largest fraction of energy is deposited as H_2O vibrational energy at all collision energies with a small participation of the translational energy, about 15% in average, in the R2 path the picture is very different. Now the largest fraction corresponds to the translation, about 50%, with a small participation of the water vibrational energy, about 20%. In addition, it is observed that the other products in each path, CH_2OH and CH_3O, respectively, receive a noticeable internal energy, i.e., they do not behave like simple spectators. The results of Table 4 suggest that although both paths, R1 and R2, are typical hydrogen abstraction reactions, different mechanisms of reaction are operating (below we will return to this point).

Figure 5 shows the energy distributions (relative translational, vibrational and rotational) of the products of reaction for both R1 and R2 paths in the OH + CH_3OH reaction. In this analysis, only the results with the DZPE constraint are analysed, because the reactive trajectories with vibrational energy below the ZPE have no quantum significance. With respect to the product relative translations distribution, for both R1 and R2 paths it shifts toward higher translational energies as the collision energy increases, being more pronounced in the case of the R2 path. The vibrational distributions of the CH_2OH product (R1 path) is broader than that corresponding to the CH_3O product (R2 path) and both are practically independent of the collision energy. A similar situation is found for the vibrational distributions of the water product in both R1 and R2 paths. Finally, the rotational distribution of the CH_2OH product (R1 path) is broader and more dependent on collision energy than that of the CH_3O product (R2 path), while for the water product in both paths the rotational distributions are practically independent of collision energy, where the rotational excitation is hotter in the R2 path. These results reinforce the idea suggested in the previous paragraph about the product energy partitioning that different mechanisms of reaction operate for the R1 and R2 paths.

Another interesting dynamics property is the product scattering distribution, which may shed light on the mechanisms of reaction. These distributions measured as differential cross sections (DCSs) are shown in Figure 6 for the R1 and R2 paths. Note that in this case, for a clearer comparison, only three collision energies, 2, 4 and 10 kcal mol^{-1}, are shown.

For the R1 path, the scattering distribution shifts from a forward-backward scattering at the lowest collision energy to a forward scattering at the highest energy. This forward behaviour is associated with a stripping mechanism, large impact parameters and a direct mechanism. By contrast, the forward-backward behaviour at lower energies is associated with a complex formation mechanism. In this case, the forward behaviour associated to a stripping mechanism with large impact parameters and the backward tendency associated to a rebound mechanism with small impact parameters. For the R2 path, the picture is different, especially at low collision energies. The angular distribution shifts from forward to sideways scattering as the collision energy increases, associated with direct mechanisms, where the participation of the complex formation mechanism is very small and only observed at the lowest collision energy.

In order to understand the different mechanisms operating for the R1 and R2 paths, Figure 7 plots the correlation between scattering angle and impact parameter. Note that only the information at collision energy of 2 kcal mol^{-1} is reported, because the differences are more notable. Clearly, two types of scattering are observed for both paths. In the R2 path an anti-correlation between impact parameters and scattering angles is observed, with large impact parameters associated to forward scattering (stripping mechanism) and small impact parameters to backward scattering (rebound mechanism). Therefore we conclude that the R2 path evolves mostly through a direct mechanism. However, in the R1 path we observe a different picture, a homogenous distribution, which is attributed to an indirect mechanism, where a large number of reactive trajectories are trapped in the intermediate complexes. It is very difficult to quantify the importance of each mechanism. Here, we obtained a first approximation to the problem for visualization of individual trajectories by using the average time of flight, <100 fs for direct and >100 fs for indirect. The latter case is related with multiple inner–outer turning points, which are absent in the direct mechanism. Note that these times of flight depend on the initial conditions of the trajectory and therefore are not absolute magnitudes. However, they provide a simple visual tool to distinguish both mechanisms. At this collision energy, 2 kcal mol^{-1}, we observe that while for the R2 path about 90 % of the reactive trajectories follow a direct mechanism, for the R1 path we found that about 35% follow a direct mechanism versus 65% with indirect mechanism. In this latter case, many reactive trajectories are trapped in the complexes along the reaction, “forgetting” the initial direction of approximation. As a consequence, an almost isotropic distribution is obtained, correlated with forward-sideways-backward scattering distributions.

V. CONCLUSIONS

The three main conclusions from the present work are summarized below. The OH + CH_3OH hydrogen abstraction reaction represents a polyatomic complex system which evolves through two paths, R1: $CH_2OH + H_2O$ and R2: $CH_3O + H_2O$. In order to describe the nuclear motion in this eight-bodies and 18 degrees of freedom system, an analytical full-dimensional potential energy surface, PES-2022, was developed as a valence bond-mechanics molecular function, which was fitted to high level *ab initio* calculations. PES-2022 reasonably simulates the *ab initio* enthalpies of reaction, stability of the complexes in the entrance and exit channels and barrier heights for both paths, which are sensitive magnitudes describing the topology of the surface. Obviously this is a test of self-consistency, but it represents a first test of quality of the new PES. As the PES-2022 surface is based on simple and physically intuitive concepts, it uses a reduced and selected number of *ab initio* calculations in the fitting, which represents an advantage with respect to other approaches.

Based on PES-2022 a QCT dynamics analysis was carried out at a temperature of 298 K for a direct comparison with experiments, which represents another stringent test of quality of the new surface. Experimentally the water product was analysed. It was found that the largest fraction of energy available was deposited as water vibrational energy, ~ 44%, and that the H_2O product vibrational population was inverted in the stretching modes and not inverted in the bending modes. PES-2022 reasonably simulates these experimental results, which lends confidence to the tools used in the present study, PES-2022, QCT and normal mode analysis (NMA method).

Finally, in order to complete the dynamics study and understand the mechanisms of reaction in the R1 and R2 paths, a QCT dynamics analysis was carried out at different collision energies. On analysing the excitation functions, the product energy partitioning in vibration, rotation and translation, and the product scattering distributions, we observe a different behaviour for both paths and conclude that different mechanisms operate for both R1 and R2 paths. While the R2 path evolves mostly through a direct mechanism, the R1 path evolves through an indirect mechanism, where a large number of reactive trajectories are trapped in the intermediate complexes along the path. Obviously, this effect is more important at low collision energies.

In sum, different severe tests have shown that PES-2022 presents great capacity and versatility to describe the dynamics behaviour of this eight-bodies reactive system, which evolves through two paths with different mechanisms.

ACKNOWLEDGEMENTS

This work was partially supported by Junta de Extremadura and European Regional Development Fund, Spain (Projects No. GR21032). The authors gratefully acknowledge the computer resources at Lusitania (COMPUTAEX) and technical support provided by COMPUTAEX. We are grateful to James McCue for assistance in language editing.

AUTHOR DECLARATIONS

Conflict of Interest

The authors have no conflicts to disclose.

Author contributions

Joaquin Espinosa-Garcia: Conceptualization (lead); Formal analysis (lead); Investigation (lead); Software (equal); Writing – original draft (equal); **Cipriano Rangel**: Conceptualization (supporting); Formal analysis (supporting); Investigation (supporting); Software (equal); Writing – original draft (equal).

REFERENCES

[1] J. Espinosa-Garcia, C. Rangel and J.C. Corchado, Molecules **27**, 3773 (2022).

[2] D. L. Baulch, C. T. Bowman, C. J. Cobos, R. A. Cox, T. Just, J. A. Kerr, M. J. Pilling, D. Stocker, J. Troe, W. Tsang, R. W. Walker, and J. Warnatz, J. Phys. Chem. Ref. Data **34**, 757–1397 (2005).

[3] R. J. Shannon, M. A. Blitz, A. Goddard, and D. E. Heard, Nat. Chem. **5**, 745–749 (2013).

[4] J. C. G. Martin, R. L. Caravan, M. A. Blitz, D. E. Heard, and J. M. C. Plane, J. Phys. Chem. A **118**, 2693–2701 (2014).

[5] K. Acharyya, E. Herbst, R. L. Caravan, R. J. Shannon, M. A. Blitz, and D. E. Heard, Mol. Phys. **113**, 2243–2254 (2015).

[6] U. Meier, H.H. Grotheen, G. Riekert and T. Just, Ber.Bunsenges Phys.Chem. **89**, 325 (1985)

[7] J.A. McCaulley, J.A. Kelly, M.F. Golde and F. Kaufmann, J.Phys.Chem. **93**, 1014-1018 (1989).

[8] B. Ruscic, R. E. Pinzon, G. von Laszewski, D. Kodeboyina, A. Burcat, D. Leahy, D. Montoy and A. F. Wagner, J. Phys.Conf. Ser., **6**, 561–570 (2005). B. Ruscic, J.Phys.Chem. A **119**, 7810-7837 (2015).

[9] L. Pardo, J.R. Banfelder and R. Osman, J. Am. Chem. Soc. **114**, 2383–2390 (1992).

[10] J. T. Jodkowski, M. T. Rayez, J. C. Rayez, T. Berces, and S. Dobe, J. Phys. Chem. A **103**, 3750–3765 (1999).

[11] A. Galano, J. R. Alvarez-Idaboy, G. Bravo-Perez, and M. E. Ruiz-Santoyo, Phys. Chem. Chem. Phys. **4**, 4648–4662 (2002).

[12] S. Xu and M. C. Lin, Proc. Combust. Inst. **31**, 159–166 (2007).

[13] K.L. Feilberg, M. Gruber-Stadler, M.S. Johnson, M. Muhlhauser and C.J. Nielsen, J.Phys.Chem. A **112**, 11099–11114 (2008).

[14] W. Siebrand, Z. Smedarchina, E. Martinez-Nuñez and A. Fernandez-Ramos, Phys. Chem. Chem. Phys. **18**, 22712–22718 (2016).

[15] L. G. Gao, J. J. Zheng, A. Fernandez-Ramos, D. G. Truhlar, and X. F. Xu, J. Am. Chem. Soc. **140**, 2906–2918 (2018).

[16] O. Roncero, A. Zanchet and A. Aguado, Phys. Chem. Chem. Phys. **20**, 25951–25958 (2018).

[17] T.L. Nguyen, B. Ruscic and J.F. Stanton, J.Chem.Phys. **150**, 084105 (2019).

[18] A.J. Ocaña, S. Blazquez, A. Potapov, B. Ballesteros, A. Canosa, M. Antiñolo, L. Vereecken, J. Albaladejo and E. Jimenez, Phys. Chem. Chem. Phys. **21**, 6942-6957 (2019).

[19] M. A. Ali, M. Balaganesh, F. A. Al-Odail1 and K. C. Lin, Scientific Reports, Nature portfolio, **11**, 12185 (2021).

[20] F. Naumkina, P. del Mazo-Sevillano, A. Aguado, Y.V. Suleimanov and O. Roncero, ACS Earth Space Chem. **3(7)**, 1158–1169 (2019).

[21] N. I. Butkovskaya and D.W. Setser, Int.Rev.Phys.Chem. **22**, 1-72 (2003).

[22] M. J. Frisch et al., Gaussian 16, Revision C.01, Gaussian, Inc., Wallingford, CT, 2016.

[23] H.-J. Werner et al., MOLPRO, version 2015.1, a package of *ab initio* programs, 2015, see http://www.molpro.net.

[24] J. Lee and R. Taylor, Int. J. Quantum Chem., **36**, 199-207 (1989).

[25] J.C. Rienstra-Kiracofe, W.D. Allen and H.F. Schaefer, J. Phys. Chem. A **104**, 9823-9840 (2000).

[26] C. Rangel, M. Garcia-Chamorro, J.C. Corchado and J. Espinosa-Garcia, Phys. Chem. Chem. Phys. **22**, 14796-14810 (2020).

[27] J. Espinosa-Garcia and J.C. Corchado, Phys. Chem. Chem. Phys. **23**, 21065-21077 (2021).

[28] C. Rangel, J. Espinosa-Garcia ad J.C. Corchado, Phys. Chem. Chem. Phys. **24**, 12501-12512 (2022).

[29] E. Gonzalez-Lavado, J.C. Corchado and J. Espinosa-Garcia, J.Chem.Phys. **140**, 064310 (2014).

[30] J.C. Corchado, J.L. Bravo and J. Espinosa-Garcia, J.Chem.Phys. **130**, 184314 (2009).

[31] R. J. Duchovic, Y. L. Volobuev, G. C. Lynch, A. W. Jasper, D. G. Truhlar, T. C. Allison, A. F. Wagner, B. C. Garrett, J. Espinosa-Garcia and J. C. Corchado, POTLIB, http://comp.chem.umn.edu/potlib.

[32] W. L. Hase, et al., VENUS96: a general chemical dynamics computer program, QCPE Bull., 1996, 16.

[33] X. Hu, W. L. Hase and Y. Pirraglia, J. Comput. Chem. **12**, 1014-1024 (1991).

[34] D. G. Truhlar and N. C. Blais, J. Chem. Phys. **67**, 1532-1537 (1977).

[35] J.C. Corchado and J. Espinosa-Garcia, Phys.Chem.Chem.Phys. **11**, 10157-10164 (2009).

[36] CH. L. Rasmussen, K.H. Wassard, K. Dam-Johansen, and P. Glarborg, Int.J.Chem.Kinet. **40**, 423-441 (2008).

Table 1. Input parameters for QCT calculations[a] for the OH + CH_3OH reaction

Parameter	OH+ CH_3OH	Explanation
Temperature, T	298	Temperature (K)
b_{max}	6.1 (R1), 6.6 (R2)	Maximum impact parameter (Å)
Trajectories	1 000 000	Number of trajectories run for each path
Reactant vibration	Thermal sampling	CH_3OH and OH vibrational energy at this temperature
Reactant rotation	Thermal sampling	CH_3OH and OH rotational energy at this temperature
Energy, E	1, 2, 3, 4, 5, 7, 10	Collision energy (kcal mol^{-1})
b_{max}	3.4, 3.3, 3.1, 3.1, 3.3, 3.3, 3.6	R1 path
	3.7, 3.6, 3.3, 3.1, 3.1, 3.1, 3.2	R2 path
Trajectories	300 000 for each energy and path	
Reactant vibration	Ground-state	
Reactant rotation	Temperature sampling at 10 K	
For both T and E		
O-C distance	15.0	Initial and final O-C separation (Å)
ε	0.1	Propagation step (fs)
Impact parameter, vibrational phases and spatial orientation	Montecarlo sampling	

a) A more complete explanation of these parameters can be found in the VENUS code manual.[32,33]

Table 2. Theoretical and experimental product energy partitioning (in percentages) for the R1 and R2 paths of the OH + CH_3OH reaction at 298 K

	R1		R2	
	QCT[a]	Exp.[b]	QCT	Exp
$f_V(CH_2OH)$	14		-	
$f_R(CH_2OH)$	19		-	
$f_V(CH_3O)$	-		7	
$f_R(CH_3O)$	-		6	
f_V(water)	44	44	27	
f_R(water)	8		19	
f_T	15		41	

a) f_V, f_R and f_T represent, respectively, the fractions of energy as vibration, rotation and translation.

b) From Ref. 21

Table 3. Theoretical H_2O vibrational distributions (%) for the R1 and R2 paths at 298 K. The experimental values[21] (in parentheses) correspond to the R1 path.

R1 path						
$v_{1,3}$	v_2=0	1	2	3	4	$P_{1,3}$
0	4 (13)	9 (9)	11 (6)	9 (4)	4 (2)	37 (35)
1	28 (29)	16 (12)	7 (8)	2		53 (49)
2	9 (9)	1 (7)				10 (16)
P_2	41 (52)	26 (28)	18 (14)	11 (4)	4 (2)	

R2 path						
$V_{1,3}$	v_2=0	1	2	3	4	$P_{1,3}$
0	29	11	2			42
1	54	2				56
2	2					2
P_2	85	13	2			

$v_{1,3} = v_1 + v_3$ combined stretch modes; v_2 bend mode.

Table 4. Product energy partitioning (in percentages) for the R1 and R2 paths of the OH + CH_3OH reaction at different collision energies (kcal mol^{-1})

R1 path					
Energy	$f_V(CH_2OH)$	$f_R(CH_2OH)$	f_V(water)	f_R(water)	f_{Transl}
E=1	12	18	50	6	14
E=2	12	18	49	7	14
E=3	14	18	45	8	15
E=4	14	19	45	7	15
E=5	15	19	44	7	15
E=7	16	21	37	8	18
E=10	16	23	34	8	19
R2 path					
Energy	$f_V(CH_3O)$	$f_R(CH_3O)$	f_V(water)	f_R(water)	f_{Transl}
E=1	6	6	26	19	43
E=2	6	6	25	19	44
E=3	7	8	19	19	47
E=4	6	9	19	19	47
E=5	7	10	19	19	50
E=7	6	10	19	19	52
E=10	5	9	16	16	54

FIGURE CAPTIONS

Figure 1. Schematic energy profiles for the R1 and R2 paths in the OH + CH_3OH reaction. Values in kcal mol^{-1} with respect to the reactants. The values correspond to PES-2022 and *ab initio* CCSD(T)-F12/aug-cc-PVTZ level.

Figure 2. R1 and R2 reaction paths. The values correspond to PES-2022 (blue) and *ab initio* CCSD(T)-F12/aug-cc-PVTZ (red). The value zero of the reaction coordinate corresponds to the saddle point, and negative (positive) values to the reactant (product) zone.

Figure 3. PES-2022 schematic 2D representations of the broken and formed bonds for the (R1) (upper panel) and (R2) (lower panel) paths. Note that the remaining coordinates are fixed at their values in their respective saddle point.

Figure 4. Reaction cross section ($Å^2$) as a function of the collision energy (kcal mol^{-1}). These values were calculated with statistical errors < 3% and are not represented; solid line, using all reactive trajectories; dashed line, using reactive trajectories with the DZPE constraint.

Figure 5. Energy distributions of the products of the OH + CH_3OH reaction at different collision energies (the lower value at 1 kcal mol^{-1} is not included because the reactivity is very small). Left column, R1 path, and right column, R2 path. In each column, from the top to bottom: relative translational energy, P(T); vibrational energy, P(v) for the CH_2OH or CH_3O products; rotational energy P(r) for the CH_2OH or CH_3O products, vibrational energy P(v) for the H_2O product and rotational energy P(r) for the H_2O product. Values obtained using the DZPE constraint. Vertical lines in the vibrational distributions indicate the ZPEs of the products in both R1 and R2 paths.

Figure 6. QCT product angular distributions for the R1 and R2 paths of the OH + CH_3OH reaction at different collision energies. Each series in these plots is normalized to unity for a clearer comparison.

Figure 7. Correlation between the impact parameter, b in Å, and the scattering angle of the H_2O product with respect to the OH free radical incident. Collision energy of 2 kcal mol^{-1} for the R1 and R2 paths.

Figure 1

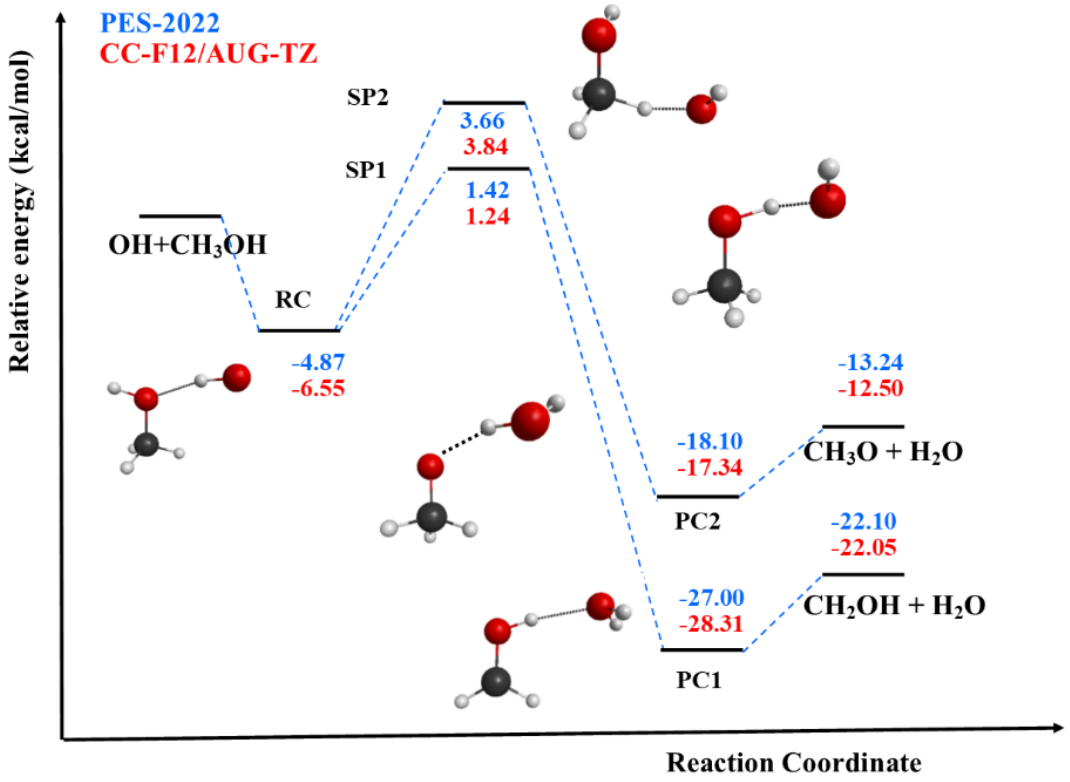
PES-2022
CC-F12/AUG-TZ
Relative energy (kcal/mol)
SP2
3.66
3.84
SP1
1.42
1.24
OH+CH3OH
RC
-4.87
-6.55
-18.10
-17.34
PC2
-13.24
-12.50
CH3O + H2O
-22.10
-22.05
CH2OH + H2O
-27.00
-28.31
PC1
Reaction Coordinate

Figure 2

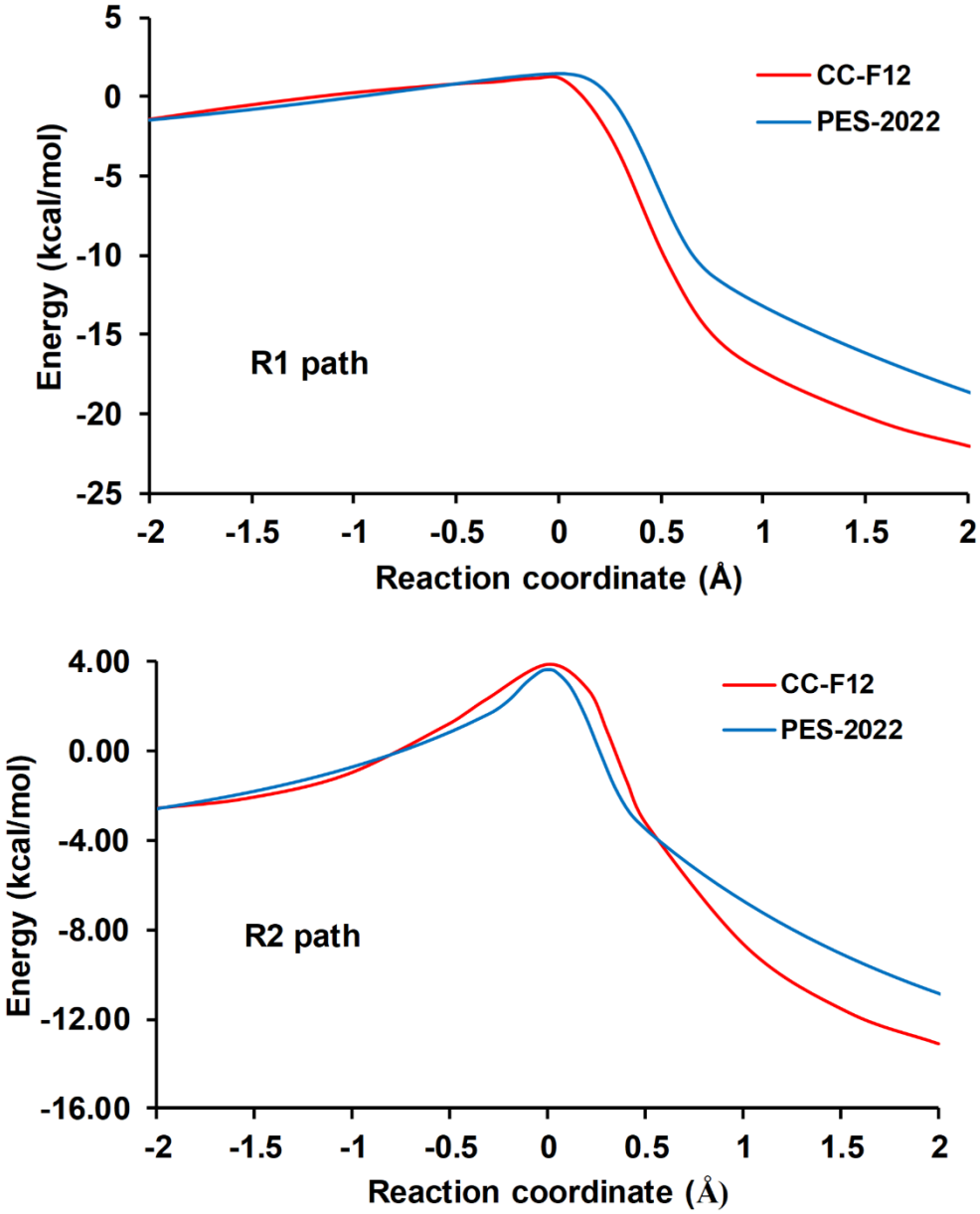
5
0
-5
-10
-15
-20
-25
Energy (kcal/mol)
CC-F12
PES-2022
R1 path
-2
-1.5
-1
-0.5
0
0.5
1
1.5
2
Reaction coordinate (Å)
4.00
0.00
-4.00
-8.00
-12.00
-16.00
Energy (kcal/mol)
CC-F12
PES-2022
R2 path
-2
-1.5
-1
-0.5
0
0.5
1
1.5
2
Reaction coordinate (Å)

Figure 3

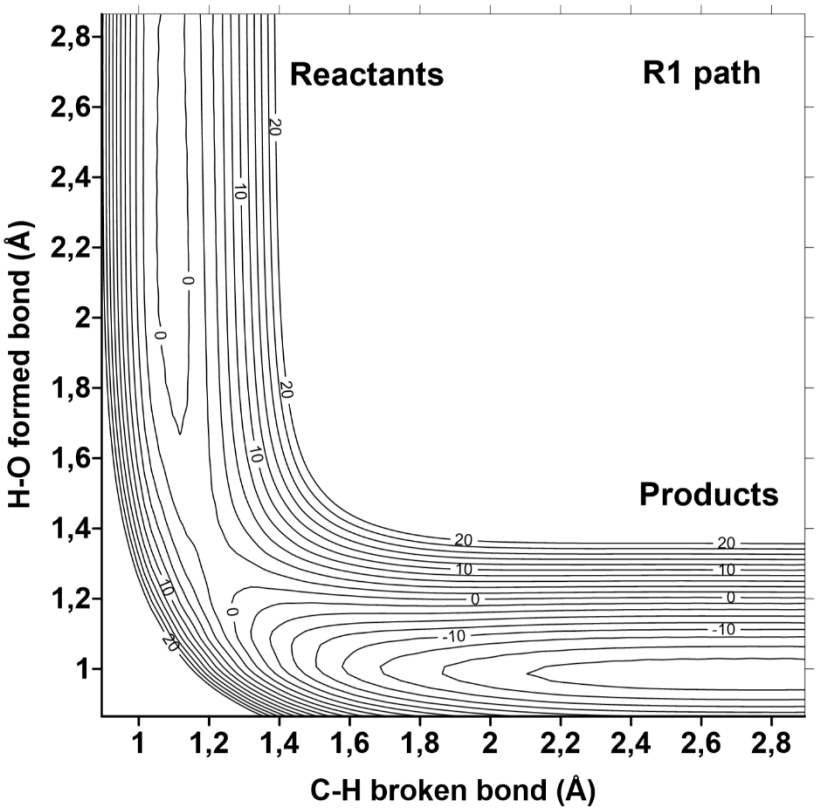
Reactants
R1 path
Products
H-O formed bond (Å)
C-H broken bond (Å)
2,8
2,6
2,4
2,2
2
1,8
1,6
1,4
1,2
1
1
1,2
1,4
1,6
1,8
2
2,2
2,4
2,6
2,8
20
10
0
-10

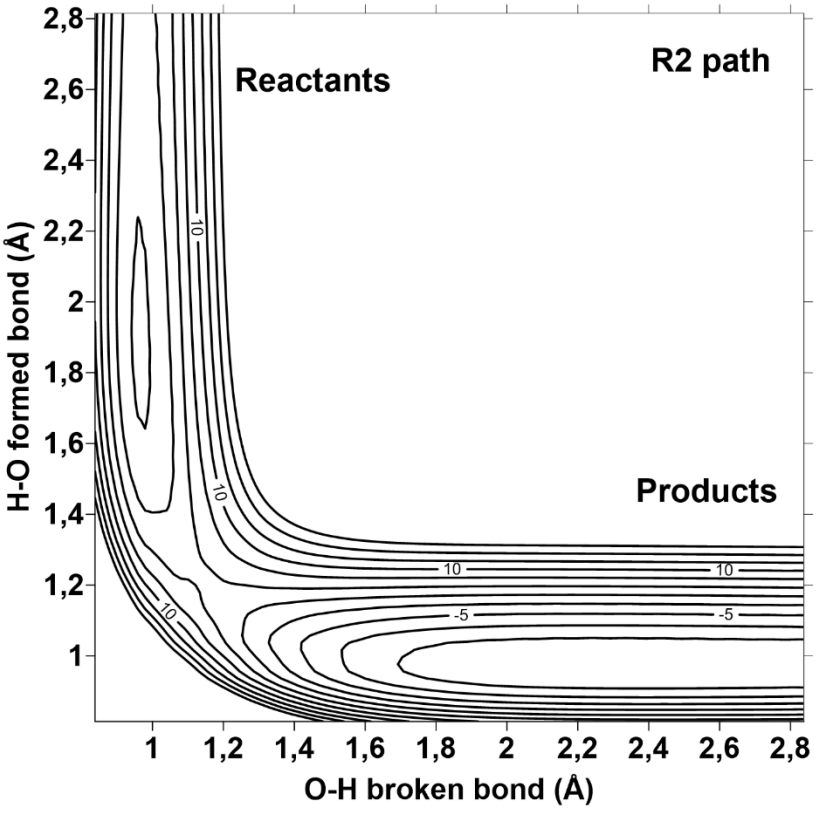
Reactants
R2 path
Products
H-O formed bond (Å)
O-H broken bond (Å)
2,8
2,6
2,4
2,2
2
1,8
1,6
1,4
1,2
1
1
1,2
1,4
1,6
1,8
2
2,2
2,4
2,6
2,8
10
-5

Figure 4

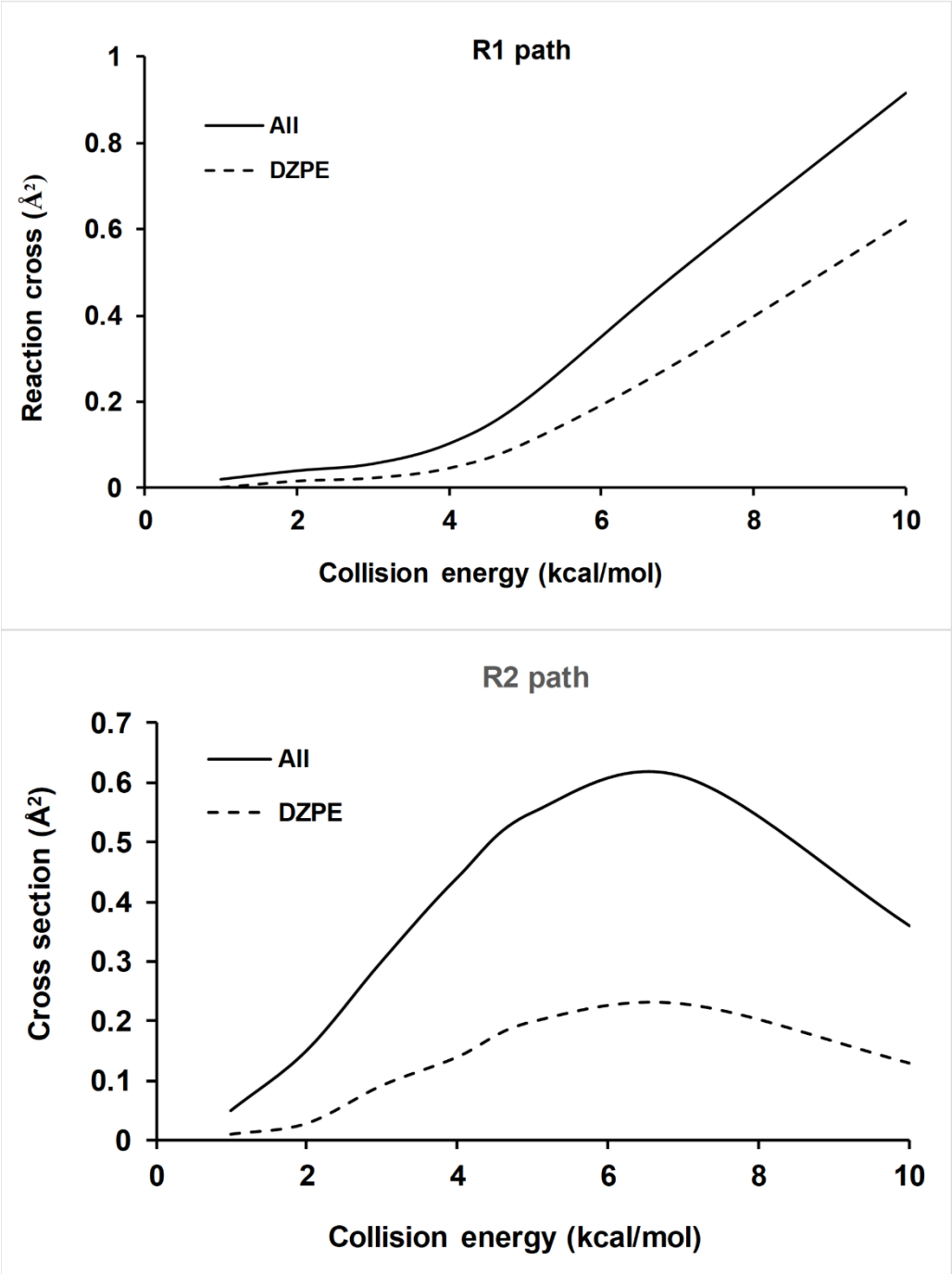
R1 path
All
DZPE
Reaction cross (Å²)
1
0.8
0.6
0.4
0.2
0
0
2
4
6
8
10
Collision energy (kcal/mol)
R2 path
All
DZPE
Cross section (Å²)
0.7
0.6
0.5
0.4
0.3
0.2
0.1
0
0
2
4
6
8
10
Collision energy (kcal/mol)

Figure 5

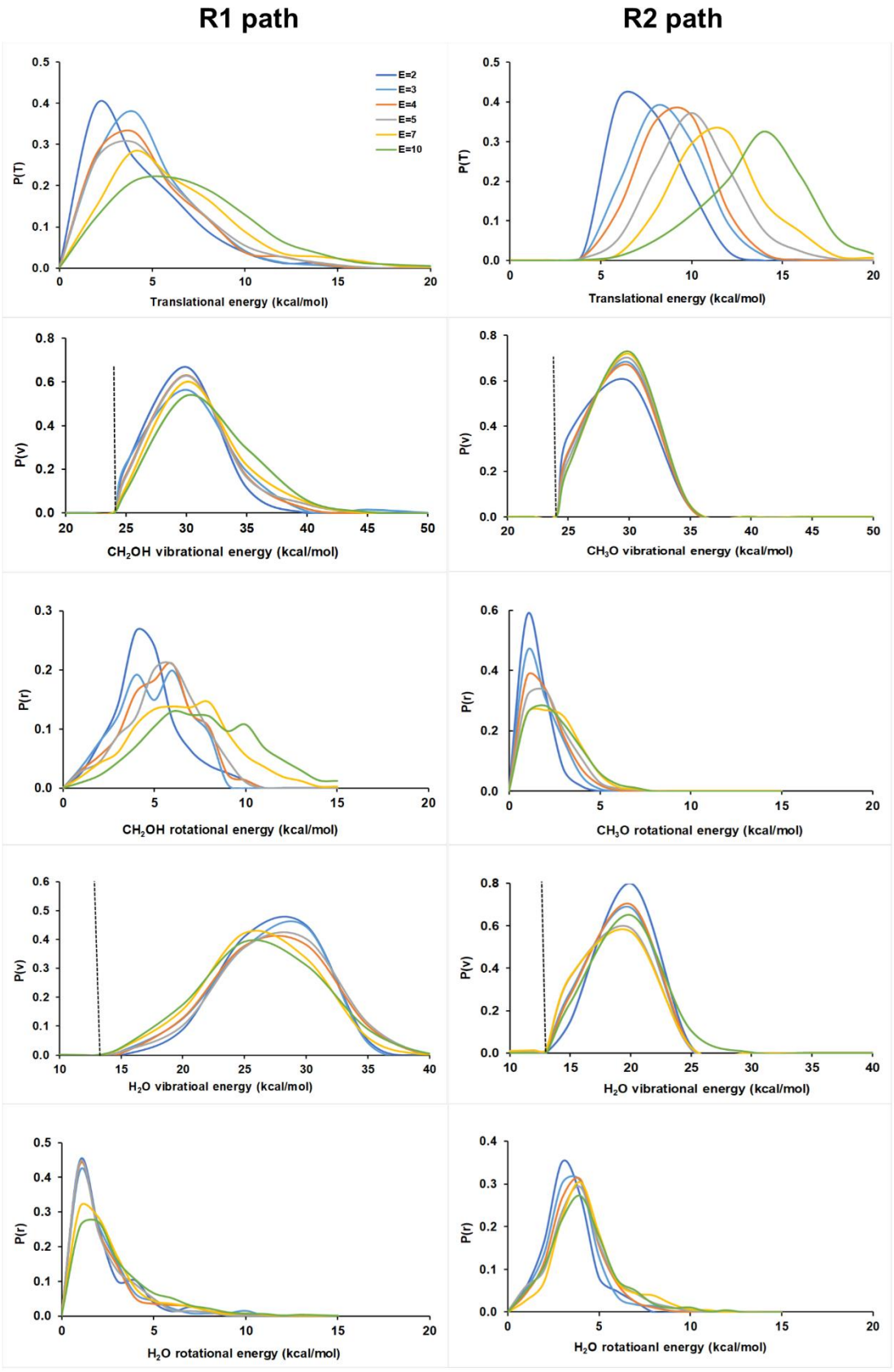
R1 path
R2 path
E=2
E=3
E=4
E=5
E=7
E=10
P(T)
Translational energy (kcal/mol)
P(v)
CH2OH vibrational energy (kcal/mol)
CH3O vibrational energy (kcal/mol)
P(r)
CH2OH rotational energy (kcal/mol)
CH3O rotational energy (kcal/mol)
H2O vibratioal energy (kcal/mol)
H2O vibrational energy (kcal/mol)
H2O rotational energy (kcal/mol)
H2O rotatioanl energy (kcal/mol)

Figure 6

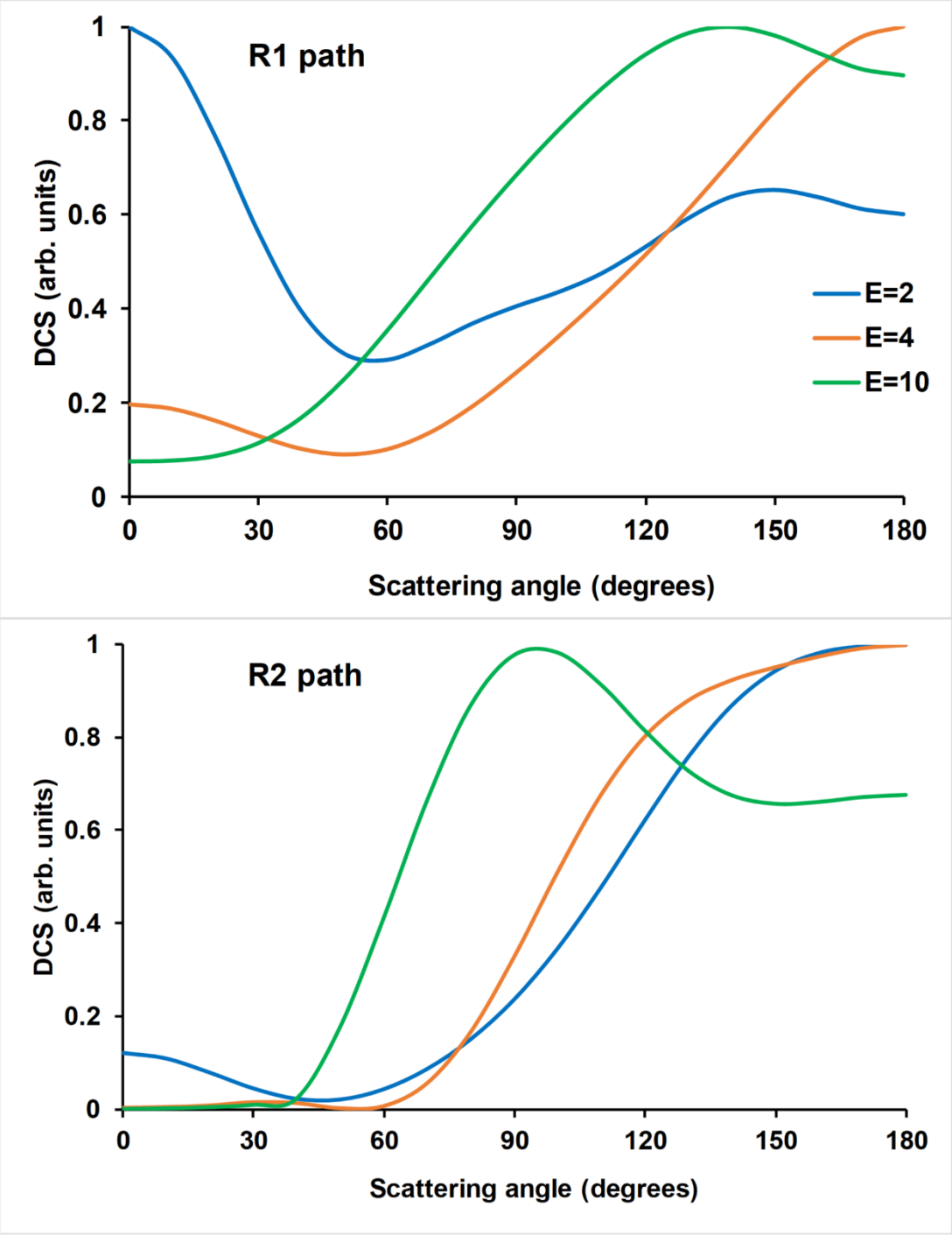
R1 path
DCS (arb. units)
Scattering angle (degrees)
E=2
E=4
E=10
R2 path
DCS (arb. units)
Scattering angle (degrees)

Figure 7

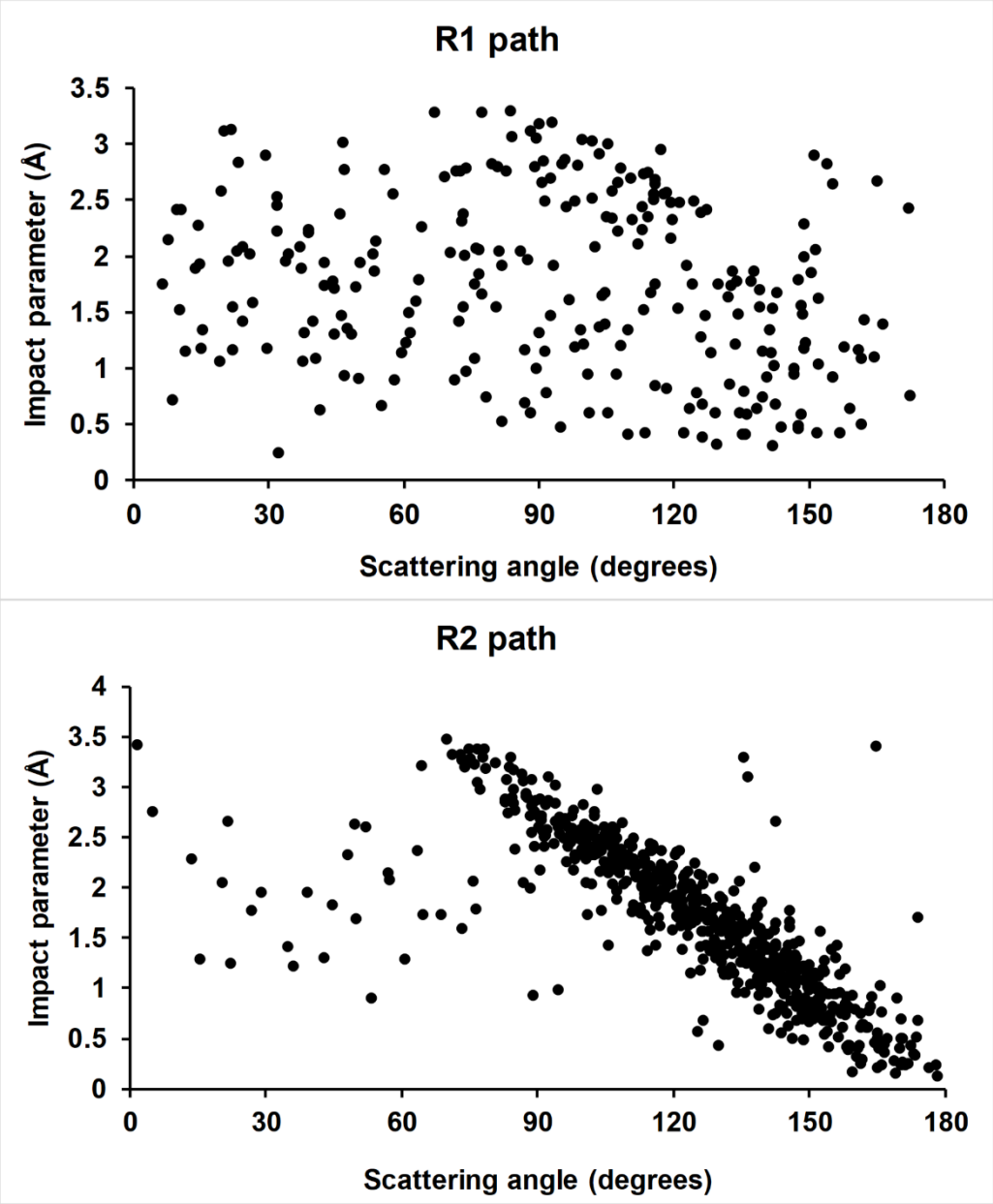
R1 path
Impact parameter (Å)
3.5
3
2.5
2
1.5
1
0.5
0
0
30
60
90
120
150
180
Scattering angle (degrees)
R2 path
Impact parameter (Å)
4
3.5
3
2.5
2
1.5
1
0.5
0
0
30
60
90
120
150
180
Scattering angle (degrees)
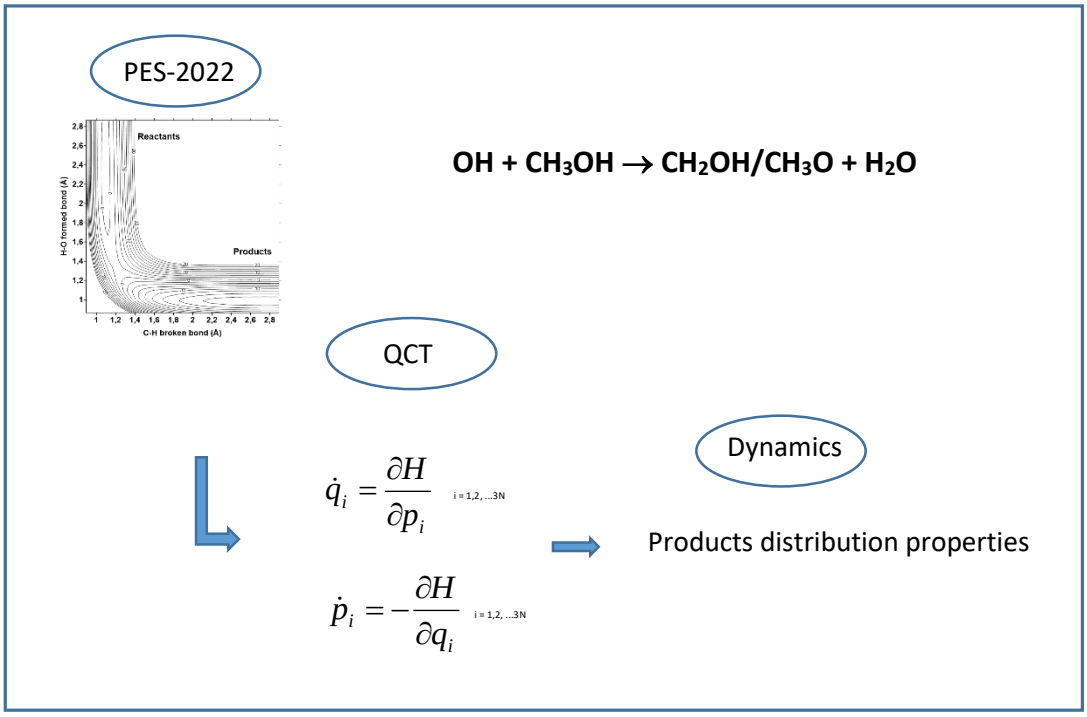
Graphical abstract